Geophysical Research Letters

RESEARCH LETTER
10.1029/2024GL108973

Thermoelastic Anomaly of Iron Carbonitride Across the Spin Transition and Implications for Planetary Cores

Shengxuan Huang[1,2], **Xiang Wu**[3], **Stella Chariton**[4], **Vitali Prakapenka**[4], **Shan Qin**[1], and **Bin Chen**[5]

[1]Key Laboratory of Orogenic Belts and Crustal Evolution, MOE, Peking University and School of Earth and Space Sciences, Peking University, Beijing, China, [2]Now at Geodynamics Research Center, Ehime University, Matsuyama, Japan, [3]State Key Laboratory of Geological Processes and Mineral Resources, China University of Geosciences, Wuhan, China, [4]Center for Advanced Radiation Sources, University of Chicago, Chicago, IL, USA, [5]Hawaiʻi Institute of Geophysics and Planetology, University of Hawaiʻi at Mānoa, Honolulu, HI, USA

Key Points:

- The *h*-type $Fe_7(N_{0.75}C_{0.25})_3$ is stable to 120 GPa and 2100 K, but undergoes a pressure-induced spin transition
- Spin transition causes a significant reduction in γ_0 and α_0, and the thermal equation of state of *h*-type non-magnetic $Fe_7(C,N)_3$ is determined
- The density profile and seismic features of a planetary core could be altered across the spin transition, which may affect core dynamics

Supporting Information:

Supporting Information may be found in the online version of this article.

Correspondence to:

B. Chen and X. Wu,
binchen@hawaii.edu;
wuxiang@cug.edu.cn

Citation:

Huang, S., Wu, X., Chariton, S., Prakapenka, V., Qin, S., & Chen, B. (2024). Thermoelastic anomaly of iron carbonitride across the spin transition and implications for planetary cores. *Geophysical Research Letters*, *51*, e2024GL108973. https://doi.org/10.1029/2024GL108973

Received 22 FEB 2024
Accepted 15 AUG 2024

Abstract

Carbon and nitrogen are considered as candidate light elements present in planetary cores. However, there is limited understanding regarding the structure and physical properties of Fe-C-N alloys under extreme conditions. Here diamond anvil cell experiments were conducted, revealing the stability of hexagonal-structured $Fe_7(N_{0.75}C_{0.25})_3$ up to 120 GPa and 2100 K, without undergoing any structural transformation or dissociation. Notably, the thermal expansion coefficient and Grüneisen parameter of the alloy exhibit a collapse at 55–70 GPa. First-principles calculations suggest that such anomaly is associated with the spin transition of iron within $Fe_7(N_{0.75}C_{0.25})_3$. Our modeling indicates that the presence of ∼1.0 wt% carbon and nitrogen in liquid iron contributes to 9–12% of the density deficit of the Earth's outer core. The thermoelastic anomaly of the Fe-C-N alloy across the spin transition is likely to affect the density and seismic velocity profiles of (C,N)-rich planetary cores, thereby influencing the dynamics of such cores.

Plain Language Summary

A significant amount of light elements are believed to be present in the cores of Earth and other planets to explain the density difference between iron-nickel alloys and geophysical observations. This study used experiments at high-pressure and high-temperature conditions and theoretical simulations to investigate a specific candidate phase of the core called $Fe_7(N_{0.75}C_{0.25})_3$, which has a hexagonal structure, at high pressures similar to those in planetary cores. This phase did not undergo any major structural changes under the conditions investigated. However, its properties related to the thermoelastic behaviors showed significant changes between 55 and 70 GPa. Theoretical calculations indicate that this anomalous behavior is linked to the magnetic transition within *h*-type $Fe_7(N_{0.75}C_{0.25})_3$. These findings suggest that the characteristics of a planetary core would be altered in the transition region, leading to a more complex thermal evolution than previously believed. This study provides insights into the behavior of light elements in planetary cores and its implications for planetary dynamics.

1. Introduction

The Earth's core is predominantly composed of iron (Fe) with approximately 5 wt% nickel (Ni) and 5–10 wt% light elements, which are necessary to account for the core density deficit (Birch, 1964; Hirose et al., 2021 and references therein). Carbon (C) is considered one of the primary candidate light elements in the Earth's and planetary cores due to its strong affinity for Fe and its high abundance in chondrites (Dasgupta & Walker, 2008; Wood, 1993). When significant amounts of carbon are alloyed with Fe to form Fe carbides, they possess ultralow shear wave velocity and high Poisson's ratio, similar to the Earth's solid inner core (Chen et al., 2014, 2018; Prescher et al., 2015). Nitrogen (N), regarded as a minor light element in planetary cores, becomes increasingly siderophile under elevated pressures (Jackson et al., 2021), suggesting its concentration in planetary cores may have been significantly underestimated. Both C and N share similar cosmochemical properties and may coexist in Fe-rich phases (Kaminsky & Wirth, 2017). Therefore, understanding the phase relations and properties of the Fe-C-N system at high pressure-temperature (*P-T*) conditions is crucial for constraining the compositions of the Earth's and planetary cores.

The phase stability of Fe carbides has been widely investigated up to pressures exceeding 200 GPa at high temperatures. The crystal structure of Fe_7C_3 under high *P-T* conditions has been proposed to be either hexagonal ($P6_3mc$, denoted as *h*-type) (Figure S1 in Supporting Information S1) or orthorhombic (*Pbca*), and the relative stabilities of these structures are still a subject of debate (Chen et al., 2012; Nakajima et al., 2011; Prescher et al., 2015). Nevertheless, the high stability and melting temperature of Fe_7C_3 have been confirmed, making it a strong candidate component for the planetary core (Liu, Lin, et al., 2016; Mashino et al., 2019). It was found that Fe-rich nitrides with diverse stoichiometries dissociate into *h*-type Fe_7N_3 above 40 GPa at elevated temperatures (Minobe et al., 2015). Our recent experiments revealed that trigonal ($P3_12$, denoted as ε-type) $Fe_7(N_{0.75}C_{0.25})_3$ transforms into an orthorhombic Fe_3C-type phase (*Pnma*, denoted as *o*-type) at ~27 GPa, and then into the *h*-type phase at ~40 GPa (Huang et al., 2021). However, the sub-solidus phase stability of ternary $Fe_7(C,N)_3$ remains unclear beyond 60 GPa. Understanding the phase stability of $Fe_7(C,N)_3$ at higher pressures is crucial for advancing our knowledge of the composition of C and N species within the planetary core.

Fe carbides and nitrides exhibit magnetic transitions under high pressure. Spectroscopic measurements have confirmed that *h*-type ferromagnetic (FM) Fe_7C_3 undergoes a transformation into a paramagnetic (PM) phase between 5.5 and 7.5 GPa, followed by a transition to a non-magnetic (NM) phase at ~53 GPa at room temperature (Chen et al., 2012). The second transition is associated with a spin transition of Fe in Fe_7C_3 (Chen et al., 2014). However, due to their unquenchable nature at ambient conditions, the spin crossover of Fe in *h*-type Fe_7N_3 or $Fe_7(N,C)_3$ has not been experimentally determined. The spin transition in ε-type Fe_7N_3 has been observed to complete at ~43 GPa and 300 K (Lv et al., 2020). Elastic properties of these binary alloys have been investigated to core pressures at room temperature (Chen et al., 2012; Lv et al., 2020; Minobe et al., 2015), revealing a magneto-elastic coupling in Fe-C-N materials. Across the spin transition, the isothermal bulk modulus (K_T) is reduced by ~15% in *h*-type Fe_7C_3, while it is elevated by ~20% in ε-type Fe_7N_3 (Chen et al., 2012; Lv et al., 2020). The thermoelastic behaviors of the *h*-type phase, however, remain largely unknown. Nakajima et al. (2011) have measured the thermal equation of state (EoS) of PM-Fe_7C_3 up to 30 GPa and 2000 K, while there are only nine high-temperature data from 40 to 130 GPa available for deriving the thermal EoS of *h*-type Fe_7N_3 (Kusakabe et al., 2019). The impact of the spin transition on the thermoelastic properties of the *h*-type phase and the thermal EoS of NM-$Fe_7(C,N)_3$ remain unresolved. These challenges limit our ability to establish accurate density profiles of Fe-C-N alloys across wide *P-T* ranges relevant to planetary cores.

In this study, we investigated the phase stability, thermoelastic properties, and spin transition of *h*-type $Fe_7(C,N)_3$ up to 120 GPa and 2100 K using synchrotron-based X-ray diffraction (XRD) in laser-heated diamond anvil cells (LHDAC) and first-principles calculations based on density functional theory (DFT). These results help to uncover the effects of spin transition and compositional variation on the thermoelastic properties of the *h*-type phase, providing new insights into the compositions and dynamical processes of the planetary cores.

2. Methods

The sample, ε-type $Fe_7(N_{0.75}C_{0.25})_3$, was synthesized at 9 GPa and 1400 K using a 2000-ton multi-anvil press. Detailed information on starting materials, the synthesis process, and sample characterization could be found in Huang et al. (2021). Symmetric DACs equipped with diamond culets of 200 μm (in run-1) and 150 μm (in run-2) in diameter were used to generate high pressures. Rhenium gaskets, initially 250 μm thick, were pre-indented into 20–25 μm in thickness. Sample chambers of 80–100 μm in diameter were laser drilled in the gaskets. Different sample loading arrangements were applied in two experimental runs (Figure S2 in Supporting Information S1). In run-1, a piece of $Fe_7(N_{0.75}C_{0.25})_3$ foil with a thickness of ~15 μm was placed on a KCl plate. Neon gas was loaded as a pressure-transmitting medium (PTM) and a pressure indicator (Fei et al., 2007). In run-2, the sample of ~10 μm in thickness was sandwiched between two KCl plates, which acted as a thermal insulator, a PTM, and a pressure indicator (Chidester et al., 2021). The sample size ($15 \times 20\ \mu m^2$) was comparable to that of the laser, which could minimize the effect of temperature gradient on the element diffusion. Note that in run-2, a small amount of MgO (capsule material for the synthesis of $Fe_7(N_{0.75}C_{0.25})_3$) was loaded into the sample chamber along with the sample, which could be identified in XRD patterns. Both runs of synchrotron XRD experiments were carried out at beamline 13-IDD, advanced photon source (APS), Argonne National Laboratory. The incident X-ray beam with a wavelength of 0.3344 Å had a focal spot size of $3 \times 4\ \mu m^2$. The samples were heated by a double-sided laser heating system with a flat-top heating spot size of ~15 μm in diameter (Prakapenka et al., 2008). Temperature was determined by fitting the thermal radiation data using the Planck radiation function under the gray body approximation. Uncertainties in temperature due to temperature gradient are estimated to be ~10% of the measured value (Kavner & Duffy, 2001). The XRD patterns were collected before, during and after heating. We followed the method proposed by Campbell et al. (2009) to estimate the effective temperature of KCl:

$$T_{\mathrm{KCl}}=\frac{3\times T_{\mathrm{meas}}+300}{4}\pm\frac{T_{\mathrm{meas}}-300}{2} \tag{1}$$

The XRD data were processed and analyzed using Dioptas (Prescher & Prakapenka, 2015) and GSAS + EXPGUI software (Toby, 2001). The *P-V* and *P-V-T* data were fitted using EoSFit7c software (Angel et al., 2014).

DFT-based first-principles calculations were performed in the Vienna ab-initio simulation package (VASP) using the projected augmented wave (PAW) method (Kresse & Joubert, 1999). The Perdew-Burke-Ernzerhof (PBE) version of the generalized gradient approximations (GGA) was chosen to treat the exchange-correlation potential (Perdew et al., 1996). Since the PBE version could predict the physical properties of Fe-rich alloys consistent with experimental results, the DFT + *U* method was not included in this study (Huang et al., 2021; Mookherjee et al., 2011). The spin-polarization of Fe without spin-orbit coupling was considered in our simulations. The FM and NM states were calculated for candidate phases. A 1 × 1 × 2 supercell was constructed to simulate the intermediate $Fe_7(N_{0.75}C_{0.25})_3$ phase. The corresponding *k*-points grids were set as 5 × 5 × 7 for the unit-cell and 5 × 5 × 3 for the supercell, respectively. Calculations were performed at various volumes, where the sub-lattice magnetic moments, atomic coordinates, and cell parameters were allowed to relax. The kinetic energy cutoff was set to 1,000 eV. The energy convergence criterion was 10^{-6} eV for the electronic self-consistent calculations.

3. Results and Discussion

3.1. Synthesis and Stability of *h*-type $Fe_7(N_{0.75}C_{0.25})_3$

Our recent experiments indicated that *ε*-type $Fe_7(N_{0.75}C_{0.25})_3$ transforms into the *h*-type structure above 40 GPa and this transition is inhibited at room temperature (Huang et al., 2021). Therefore, we first synthesized *h*-type $Fe_7(N_{0.75}C_{0.25})_3$ in DACs at 40–50 GPa under high temperature. In run-1, the sample was directly compressed to ~42 GPa at ambient temperature and then laser-heated at ~1500 K. The new diffraction peaks could be assigned to the *h*-type structure with lattice parameters $a = 6.573(2)$ Å, $c = 4.272(4)$ Å, and $V = 159.8(2)$ Å^3 at 48.1(1.0) GPa and 300 K (Figure 1a). In run-2, *h*-type $Fe_7(N_{0.75}C_{0.25})_3$ was synthesized at ~50 GPa and ~1400 K (Figure 1b). Its lattice parameters were $a = 6.562(2)$ Å, $c = 4.255(1)$ Å, and $V = 158.66(7)$ Å^3 at 52.0(1.0) GPa after quenching.

After successfully synthesizing *h*-type $Fe_7(N_{0.75}C_{0.25})_3$, we investigated its stability at higher *P-T* conditions. In run-1, we performed XRD mapping on the heating area of 18 × 24 μm^2 and selected one position with the strongest diffraction peaks of the sample. The *h*-type $Fe_7(N_{0.75}C_{0.25})_3$ was compressed at room temperature to 74.1(5) GPa. In run-2, we conducted five sets of heating cycles in the pressure range from 50 to 120 GPa. No new Bragg peaks appeared in XRD patterns in both experimental runs, indicating no structural transformation or dissociation up to 118 GPa and 2100 K (Figure 1, Figure S3 and Text S1 in Supporting Information S1).

3.2. Thermoelastic Anomaly of *h*-type $Fe_7(N_{0.75}C_{0.25})_3$

The lattice parameters of *h*-type $Fe_7(N_{0.75}C_{0.25})_3$ at extreme conditions are summarized in Tables S1–S2 in Supporting Information S1. Compared with our previous results (Huang et al., 2021), the volumes obtained in this study are 0.1–0.5% larger than those obtained in the externally-heated DAC experiment but well consistent with those in the LHDAC experiment, which should be primarily attributed to the small variation (the total contents of C and N ranging from 29.7 at% to 30.7 at%) in chemical compositions of the sample, and secondarily to different PTMs (Figures S4–S6 and Text S2 in Supporting Information S1). Since previous LHDAC data are consistent with the present results, they are used in the EoS fitting. The pressures at high temperatures are re-calibrated based on the thermal EoS of KCl reported by Chidester et al. (2021) (Figure S7 in Supporting Information S1).

The unit-cell volumes of *h*-type $Fe_7(N_{0.75}C_{0.25})_3$ at 300 K decrease with increasing pressure without any obvious discontinuity up to 112 GPa (Figure S5 in Supporting Information S1). In contrast, the normalized stress (F_E) versus Eulerian strain (f_E) plot displays a slope change at $f_E = 0.049$ (corresponding to ~53 GPa) (Figure S8a in Supporting Information S1), which is similar to the case of *h*-type Fe_7C_3 (Chen et al., 2012). This indicates that *h*-type $Fe_7(N_{0.75}C_{0.25})_3$ likely undergoes a second-order PM-NM transition at ~53 GPa and 300 K. The data below 53 GPa and above 53 GPa are fitted to the Birch-Murnaghan (B-M) EoS for the PM and NM phases, respectively (Text S3 in Supporting Information S1). Due to limited data below 53 GPa, we assume that the zero-pressure isothermal bulk modulus (K_0) and its first pressure derivative (K_0') of PM-$Fe_7(N_{0.75}C_{0.25})_3$ are the same

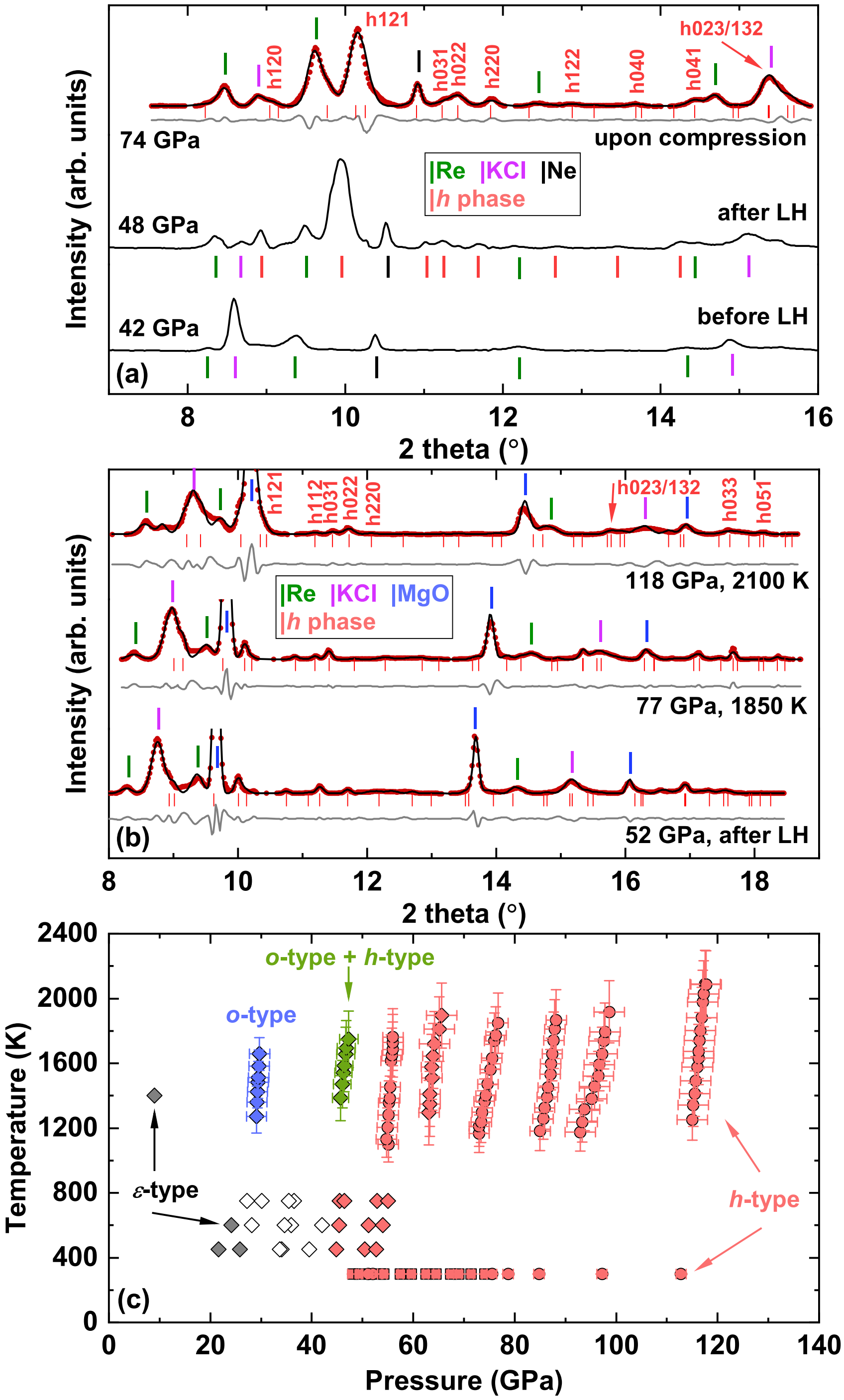

Figure 1. Representative measured X-ray diffraction (XRD) patterns of $Fe_7(N_{0.75}C_{0.25})_3$ in run-1 (a) and run-2 (b). Le Bail refinements (black curves) of observed XRD data (red dots) were carried out after background subtraction. The red, pink, black, green, and blue ticks represent Bragg peaks of *h*-type $Fe_7(N_{0.75}C_{0.25})_3$, KCl, Ne, Re, and MgO phases, respectively. The red numbers represent the characteristic peaks of *h*-type $Fe_7(N_{0.75}C_{0.25})_3$. Full peaks of *h*-type $Fe_7(N_{0.75}C_{0.25})_3$ are displayed by red ticks only for those shown with Le Bail refinements. Otherwise, only characteristic peaks of each phase are displayed by ticks. (c) Phase diagram of $Fe_7(N_{0.75}C_{0.25})_3$ at high *P*-*T* conditions. The *ε*-type, *o*-type, and *h*-type represent the $P3_12$, Fe_3C-type (*Pnma*), and Fe_7C_3-type ($P6_3mc$) phases, respectively. Diamond symbols represent data extracted from Huang et al. (2021).

as those of PM-Fe_7C_3 (K_0 = 201 GPa and K_0' = 8.0) (Chen et al., 2012), and get zero-pressure volume (V_0) as 183.8(2) $Å^3$. For the NM phase, K_0' is fixed to 3.2 using the same value as NM-Fe_7C_3 (Chen et al., 2012), and the fitted parameters for NM-$Fe_7(N_{0.75}C_{0.25})_3$ are V_0 = 182.4(5) $Å^3$ and K_0 = 302(7) GPa.

Having established the room-temperature EoS, we further derive the thermoelastic parameters of *h*-type $Fe_7(N_{0.75}C_{0.25})_3$ by fitting *P-V-T* data using the thermal pressure model. The thermal pressure is obtained with two different approaches: (a) The αK_T model and (b) the Mie-Grüneisen-Debye (MGD) model. Figure S8b in Supporting Information S1 demonstrates that the F_E values of the high-temperature data above 70 GPa are much lower than those below 70 GPa, indicating that these data cannot be fitted to a single EoS.

In the αK_T model, the αK_T value is considered to be constant above the Debye temperature if the anharmonic and electronic contributions could be neglected (Text S3 in Supporting Information S1). The thermal pressure increases almost linearly with temperature, implying no temperature dependence of αK_T (Figure 2a). However, our experimental data demonstrate a pressure dependence of the thermal pressure. The thermal pressures at ~55 GPa are close to those at ~45 GPa. They reduce by 20–25% at ~65 GPa, and by ~50% above 70 GPa. These results indicate that under high temperature iron in *h*-type $Fe_7(N_{0.75}C_{0.25})_3$ should be in the high-spin (HS) state at 45–55 GPa, in the mixed-spin (MS) state at ~65 GPa and in the low-spin (LS) state above 70 GPa. A least-squares fit to the data yields a slope (αK_T) of 0.011(1) GPa/K for the HS phase and 0.0059(1) GPa/K for the LS phase. The corresponding zero-pressure thermal expansion coefficient α_0 is calculated from αK_T and K_0 values to be $5.4(4) \times 10^{-5}$ K^{-1} for the HS phase and $2.0(2) \times 10^{-5}$ K^{-1} for the LS phase, respectively. The α_0 of HS-$Fe_7(N_{0.75}C_{0.25})_3$ is comparable to previous results for PM-Fe_7C_3 ($3.5 \sim 4.7 \times 10^{-5}$ K^{-1}) (Lai et al., 2018; Litasov et al., 2015), but much larger than that of LS-$Fe_7(N_{0.75}C_{0.25})_3$. This indicates a considerable reduction in α_0 due to the spin transition.

The *P-V-T* data were also fitted to the MGD EoS (Text S3 in Supporting Information S1) (I. Jackson & Rigden, 1996). The data collected above 70 GPa were fitted for the LS phase (Figure 2b). The Debye temperature θ_0 of *h*-type $Fe_7(N_{0.75}C_{0.25})_3$ is assumed the same as that of pure Fe (417 K), similar to the previous studies for other Fe-rich alloys (Dewaele et al., 2006; Thompson et al., 2020). A least-squares fit gives the ambient Grüneisen parameter γ_0 = 1.3(2) and q = 1.0(4). The data collected at 45–55 GPa were fitted for the HS phase, yielding γ_0 = 2.6(3) with a fixed q value of 1.0. The γ_0 of HS-$Fe_7(N_{0.75}C_{0.25})_3$ is also close to that of PM-Fe_7C_3 (Nakajima et al., 2011), but nearly twice the γ_0 of LS-$Fe_7(N_{0.75}C_{0.25})_3$. This implies a significant drop in γ_0 across the HS-LS transition. Kusakabe et al. (2019) report that γ_0 and q of Fe_7N_3 are 2.1(3) and 4.5(9), respectively, much larger than our results. We notice that their volume data at 40–60 GPa are abnormally larger than those above 70 GPa. Fitting these data to a single EoS should be thermodynamically invalid.

To further look into the effect of pressure on the thermoelastic properties of *h*-type $Fe_7(N_{0.75}C_{0.25})_3$, the thermal expansion coefficients of a^3 and c^3 are calculated (Figure 2c, Figures S9–S10 and Text S4 in Supporting Information S1). The thermal expansion coefficients are $\alpha_a = 2.3–3.0 \times 10^{-5}$ K^{-1} and $\alpha_c = 1.6–2.6 \times 10^{-5}$ K^{-1} at 45–55 GPa. At ~65 GPa, α_a significantly decreases and α_c slightly reduces. Above 70 GPa, α_a and α_c are $\sim 1.2 \times 10^{-5}$ K^{-1} and $\sim 1.0 \times 10^{-5}$ K^{-1}, respectively.

In summary, our experimental results have shown that the thermal expansions of volume and two axes and Grüneisen parameter of *h*-type $Fe_7(N_{0.75}C_{0.25})_3$ collapse between 55 and 70 GPa. In particular, the thermal expansion contrast between two axes considerably reduces above 70 GPa.

3.3. Mechanism for Thermoelastic Anomaly of *h*-type $Fe_7(N_{0.75}C_{0.25})_3$

To reveal the mechanism for the thermoelastic differences observed in our data between 55 and 70 GPa, we have performed ab initio calculations to study the magnetic properties of the *h*-type solid solution. The average magnetic moments collapse at 74 GPa for Fe_7N_3, at 76 GPa for $Fe_7(N_{0.75}C_{0.25})_3$ and at 80 GPa for Fe_7C_3 (Figure S11a in Supporting Information S1). Correspondingly, the magnetic moments of Fe at each equivalent site drop to zero indicating the spin transition of Fe from the HS state to the LS state (Figure S11 in Supporting Information S1). The substitution of C by N in the *h*-type phase slightly reduces the transition pressure.

The predicted spin transition pressure of Fe_7C_3 is consistent with the previously calculated result (Mookherjee et al., 2011). FM-Fe_7C_3 is reported to transform into the PM state at 7–20 GPa at room temperature (Chen et al., 2012; Prescher et al., 2015). We did not consider the PM state in static calculations. But note that Fe of PM-Fe_7C_3 is still in the HS state. Our predicted spin transition pressure of Fe_7C_3 is higher than the experimental result

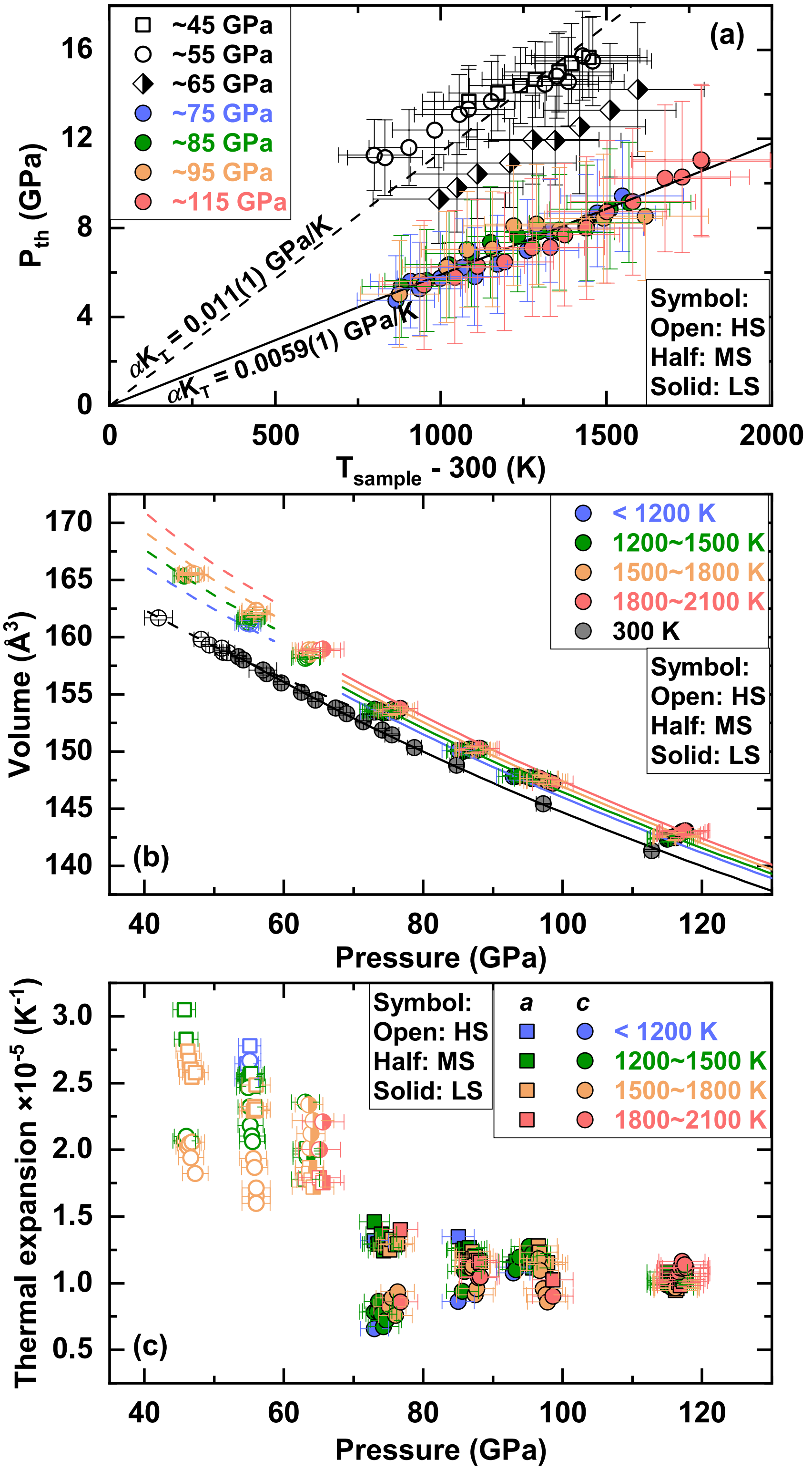

Figure 2. (a) Thermal pressure as a function of ΔT ($\Delta T = T_{sample} - 300$). The dashed and solid lines in panel (a) are calculated using the linear equation. (b) *P-V-T* data of *h*-type $Fe_7(N_{0.75}C_{0.25})_3$. The dashed and solid curves plotted in panel (b) are calculated using the MGD equation of state parameters of *h*-type HS- and LS-$Fe_7(N_{0.75}C_{0.25})_3$, respectively. (c) Thermal expansion of a^3 and c^3 of *h*-type $Fe_7(N_{0.75}C_{0.25})_3$ as a function of pressure. HS, MS and LS represent the high-spin, mixed-spin and low-spin states, respectively.

(∼53 GPa) obtained at 300 K (Chen et al., 2014). The zero-pressure magnetic moment of Fe_7C_3 is calculated to be 1.7 μ_B at 0 K, larger than the value (1.3 μ_B) measured at ambient conditions (Tsuzuki et al., 1984). This phenomenon is also found in other Fe-rich alloys, such as ε-type Fe_3N_{1+x} and Fe_3P (Gu et al., 2014; Huang et al., 2021; Lei et al., 2018; Lisher et al., 1974). This may indicate that DFT simulations are likely to overestimate the stability field of the FM state of Fe-rich alloys or that the temperature effect tends to suppress the spin of Fe (Gu et al., 2014; Tagawa et al., 2022). Therefore, the spin transition pressure predicted by static DFT simulations would be higher than that measured at room temperature. Moreover, the calculations show that the compositional variation has a negligible effect on the transition pressure. Taking all these effects into account, our calculated results support the experimental observation that *h*-type $Fe_7(N_{0.75}C_{0.25})_3$ undergoes a spin transition at ∼53 GPa at 300 K.

Our calculations show that the Fe-Fe distance in the *ab* plane (i.e., 2.403 Å at ∼49 GPa) is shorter than that along the *c* axis (i.e., 2.498 Å at ∼49 GPa) in the *h*-type structure, indicating stronger magnetic interactions in the *ab* plane than along the *c* axis for the HS state. Therefore, α_a is much larger than α_c for HS-$Fe_7(N_{0.75}C_{0.25})_3$, resulting in a considerable increase in the *a*/*c* ratio with increasing temperature at 45–55 GPa (Figure S10 in Supporting Information S1). α_a becomes comparable to α_c after the spin transition of Fe because the magnetic interactions collapse. Correspondingly, the *a*/*c* ratio is nearly independent of temperature above 70 GPa (Figure S10 in Supporting Information S1).

4. Geophysical Implications

The Earth's liquid outer core is ∼10% less dense than liquid Fe, suggesting that a substantial amount of light elements are present in the liquid core (Birch, 1964; Hirose et al., 2021 and references therein). Here we consider the scenario at the Earth's core-mantle boundary (CMB). This analysis requires only small extrapolations in pressure and temperature to apply our EoS parameters of the *h*-type LS phase at conditions of the CMB. The density of the outer core is 9.9 g/cm^3 at the CMB based on the PREM model (Dziewonski & Anderson, 1981). The pressure and temperature of the outer core at the CMB are taken to be 135.8 GPa and 4,000 ± 500 K, respectively. In addition, we apply a 1–2% volume expansion upon melting for Fe and Fe-rich alloys at the CMB pressure (Anderson, 2003). To account for the outer core's density deficit, the liquid core should contain a total concentration of 8.9–10.2 wt% C and N for a 2% volume change on melting or 10.2–11.7 wt% for a 1% volume change on melting (Figure 3a). However, the total concentration of C and N in the bulk core might be an order of ∼1.0 wt% based on their partitioning behaviors during core-mantle differentiation (Dalou et al., 2017; Fischer et al., 2020; Grewal et al., 2019, 2021; Jackson et al., 2021). The presence of ∼1.0 wt% C and N decreases the density of liquid Fe by 0.09–0.11 g/cm^3, contributing to 9–12% of the outer core's density deficit. If the thermal EoS of the HS phase were applied in the extrapolation, liquid Fe would be less dense by 15–19% with the incorporation of ∼1.0 wt% C and N. In this case, the contribution of C and N to the density deficit of the Earth's outer core is overestimated by approximately 50%. Our modeling results not only show that C and N cannot be the dominant light elements in the Earth's liquid core but also underline the significance of using proper thermodynamic parameters to extrapolate low-pressure results to more extreme conditions.

The solidification of the *h*-type phase from the Earth's liquid core requires a content of 2–3 wt% C and N in the Earth's outer core (Fei & Brosh, 2014; Mashino et al., 2019). This value is much higher than that derived from the metal-silicate partitioning data, making *h*-type $Fe_7(C,N)_3$ unlikely a dominant constituent in the Earth's inner core. However, if a terrestrial planet is accreted predominantly from (C,N)-rich building blocks (i.e., carbonaceous chondrites), such planetary core may have sufficient amounts of C and N to form *h*-type $Fe_7(C,N)_3$. Furthermore, astrophysical evidence has shown that in the extra-solar system, some stars have high C/O ratios such that the planets that they host would have a carbide-enriched metallic core (Bond et al., 2010). The alteration of physical properties of the *h*-type phase will have significant effects on the characteristics and evolution of such planets.

We have plotted the density profiles of *h*-type $Fe_7(N_{0.75}C_{0.25})_3$ at different temperatures (Figure 3b). The density of *h*-type $Fe_7(N_{0.75}C_{0.25})_3$ increases with increasing pressure at 300 K without any observable discontinuity. In contrast, the evolution of the density with pressure is not smooth under high temperature since the thermal expansion is reduced substantially after the spin transition. The density of the LS phase is 9.24 g/cm^3 at 70 GPa and 1500 K and that of the HS phase is extrapolated to be 9.11 g/cm^3 at the same conditions. The density is elevated by 1.4% across the spin transition. At 70 GPa and 2100 K, the densities are calculated to be 9.17 g/cm^3 and 9.00 g/cm^3 for the LS and HS phases, respectively, presenting a 1.8% density contrast. Such abrupt density

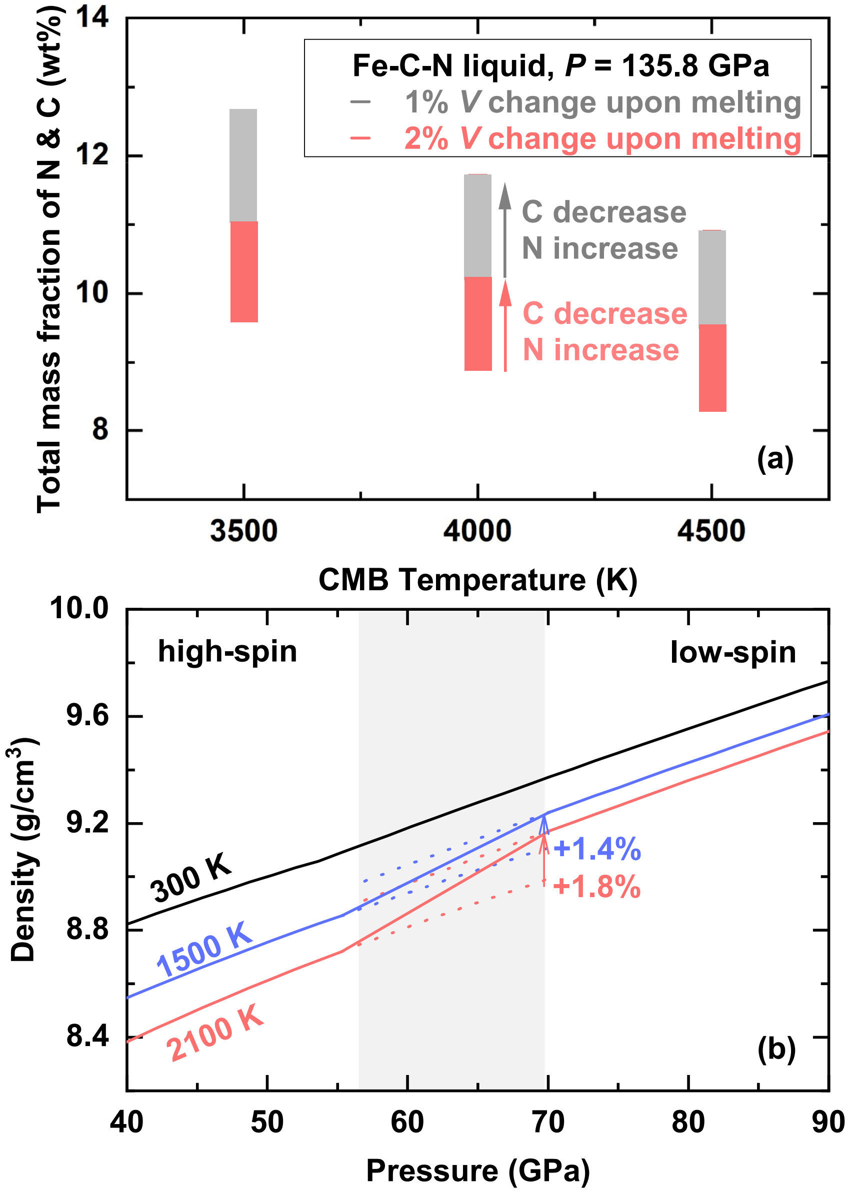

Figure 3. (a) Trade-off between temperature and the total amount of N and C required in liquid Fe to match the density deficit of the Earth's outer core at conditions of the core-mantle boundary. (b) Calculated isothermal density profiles of *h*-type $Fe_7(N_{0.75}C_{0.25})_3$ based on this study as a function of pressure at 300 K (black), 1500 K (blue), and 2100 K (red).

jump may not be observed as the spin transition is supposed to broaden significantly under high temperature. Instead, the slope of the density evolution with pressure changes considerably across the spin transition, which may be seismically detectable. This transition also leads to elastic softening in *h*-type Fe_7C_3 with large decreases in K_T and seismic velocities at 300 K (Chen et al., 2012, 2014). The adiabatic bulk modulus (K_S) is equal to $K_S = K_T(1 + \alpha\gamma T)$. Provided that both α and γ collapse after the spin transition, the reduction in the P wave velocity $\left(V_P = \sqrt{\left(K_S + \frac{4}{3}G\right)/\rho}\right)$ of the *h*-type phase is anticipated to be enhanced under high *P*-*T* conditions. Furthermore, the thermal conductivity (κ) in the planetary core plays a key role in controlling the core dynamics. It is accepted that a large γ normally indicates a low κ, though the quantitative relationship between two parameters remains to be determined (Zhou et al., 2022 and references therein). The κ of the *h*-type phase is, therefore, likely to increase after the spin transition. If the *h*-type phase is one of the dominant phases in a planetary core and the spin transition occurs in this region, the thermal evolution and cooling history of such planetary core should be more complex.

Finally, it is reported that the α_0 of NM-Fe_3S is ∼30% smaller than that of the FM phase (Thompson et al., 2020). In terms of FeH, the temperature-induced volume expansion above 40 GPa is much smaller than that at 40 GPa, at which it undergoes a spin transition (Tagawa et al., 2022). These results together indicate that the spin transition-induced thermoelastic anomaly is likely a universal phenomenon in Fe-rich alloys, but the extent of such anomaly should vary for Fe-rich compounds alloying with different light elements. Investigating the effect of spin transition on the elastic and transport properties of other Fe-rich alloys at simultaneous high-pressure and high-temperature conditions will contribute to a better understanding of the evolution of the cores of various types of planets.

Data Availability Statement

All the data necessary to produce the results are available at Huang, S. et al. (2024).

Acknowledgments

We acknowledge the financial support from the National Natural Science Foundation of China (NSFC) Grant (42225202) to XW, NSFC-42072047 to SQ. This work was in part supported by National Science Foundation (NSF) Grants (EAR-1555388, EAR-1829273, EAR-2127807) to BC. SH acknowledges support from Peking University Boya Postdoctoral Fellowship and China Postdoctoral Science Foundation (No. 2022M710194). We thank Yungui Liu, Xiang Li and Haipeng Song for their help in DAC preparations. The experiments were performed at GeoSoilEnviroCARS (Sector 13), APS, Argonne National Laboratory (ANL). GeoSoilEnviroCARS is supported by the NSF-Earth Sciences (EAR-1634415). Use of the COMPRES-GSECARS gas loading system was supported by COMPRES under NSF Cooperative Agreement EAR -1606856 and by GSECARS through NSF Grant EAR-1634415 and DOE Grant DE-FG02-94ER14466. This research used resources of the APS, a U.S. Department of Energy (DOE) Office of Science User Facility operated for the DOE Office of Science by ANL under Contract No. DE-AC02-06CH11357.

References

Anderson, O. L. (2003). The three-dimensional phase diagram of iron. In V. Dehant (Ed.), et al. (Eds.), *Earth's core: Dynamics, structure, rotation* (pp. 83–103). AGU.

Angel, R. J., Alvaro, M., & Gonzalez-Platas, J. (2014). EosFit7c and a Fortran module (library) for equation of state calculations. *Zeitschrift für Kristallographie*, *229*(5), 405–419. https://doi.org/10.1515/zkri-2013-1711

Birch, F. (1964). Density and composition of mantle and core. *Journal of Geophysical Research*, *69*(20), 4377–4388. https://doi.org/10.1029/JZ069i020p04377

Bond, J. C., O'Brien, D. P., & Lauretta, D. S. (2010). The compositional diversity of extrasolar terrestrial planets. I. In situ simulations. *The Astrophysical Journal*, *715*(2), 1050–1070. https://doi.org/10.1088/0004-637X/715/2/1050

Campbell, A. J., Danielson, L., Righter, K., Seagle, C. T., Wang, Y., & Prakapenka, V. B. (2009). High pressure effects on the iron-iron oxide and nickel-nickel oxide oxygen fugacity buffers. *Earth and Planetary Science Letters*, *286*(3–4), 556–564. https://doi.org/10.1016/j.epsl.2009.07.022

Chen, B., Gao, L., Lavina, B., Dera, P., Alp, E. E., Zhao, J., & Li, J. (2012). Magneto-elastic coupling in compressed Fe_7C_3 supports carbon in Earth's inner core. *Geophysical Research Letters*, *39*(18), L18301. https://doi.org/10.1029/2012GL052875

Chen, B., Lai, X., Li, J., Liu, J., Zhao, J., Bi, W., et al. (2018). Experimental constraints on the sound velocities of cementite Fe_3C to core pressures. *Earth and Planetary Science Letters*, *494*, 164–171. https://doi.org/10.1016/j.epsl.2018.05.002

Chen, B., Li, Z., Zhang, D., Liu, J., Hu, M. Y., Zhao, J., et al. (2014). Hidden carbon in Earth's inner core revealed by shear softening in dense Fe_7C_3. *Proceedings of the National Academy of Sciences* (Vol. 111(50), 17755–17758). https://doi.org/10.1073/pnas.1411154111

Chidester, B. A., Thompson, E. C., Fischer, R. A., Heinz, D. L., Prakapenka, V. B., Meng, Y., & Campbell, A. J. (2021). Experimental thermal equation of state of B2-KCl. *Physical Review B*, *104*(9), 094107. https://doi.org/10.1103/PhysRevB.104.094107

Dalou, C., Hirschmann, M. M., von der Handt, A., Mosenfelder, J., & Armstrong, L. S. (2017). Nitrogen and carbon fractionation during core-mantle differentiation at shallow depth. *Earth and Planetary Science Letters*, *458*, 141–151. https://doi.org/10.1016/j.epsl.2016.10.026

Dasgupta, R., & Walker, D. (2008). Carbon solubility in core melts in a shallow magma ocean environment and distribution of carbon between the Earth's core and the mantle. *Geochimica et Cosmochimica Acta*, *72*(18), 4627–4641. https://doi.org/10.1016/j.gca.2008.06.023

Dewaele, A., Loubeyre, P., Occelli, F., Mezouar, M., Dorogokupets, P. I., & Torrent, M. (2006). Quasihydrostatic equation of state of iron above 2 Mbar. *Physical Review Letters*, *97*(21), 215504. https://doi.org/10.1103/PhysRevLett.97.215504

Dziewonski, A. M., & Anderson, D. L. (1981). Preliminary reference Earth model. *Physics of the Earth and Planetary Interiors*, *25*(4), 297–356. https://doi.org/10.1016/0031-9201(81)90046-7

Fei, Y., & Brosh, E. (2014). Experimental study and thermodynamic calculations of phase relations in the Fe-C system at high pressure. *Earth and Planetary Science Letters*, *408*, 155–162. https://doi.org/10.1016/j.epsl.2014.09.044

Fei, Y., Ricolleau, A., Frank, M., Mibe, K., Shen, G., & Prakapenka, V. (2007). Toward an internally consistent pressure scale. *Proceedings of the national academy of Sciences* (Vol. 104(22), 9182–9186). https://doi.org/10.1073/pnas.0609013104

Fischer, R. A., Cottrell, E., Hauri, E., Lee, K. K., & Le Voyer, M. (2020). The carbon content of Earth and its core. *Proceedings of the national academy of Sciences* (Vol. 117(16), 8743–8749). https://doi.org/10.1073/pnas.1919930117

Grewal, D. S., Dasgupta, R., Hough, T., & Farnell, A. (2021). Rates of protoplanetary accretion and differentiation set nitrogen budget of rocky planets. *Nature Geoscience*, *14*(6), 369–376. https://doi.org/10.1038/s41561-021-00733-0

Grewal, D. S., Dasgupta, R., Sun, C., Tsuno, K., & Costin, G. (2019). Delivery of carbon, nitrogen, and sulfur to the silicate Earth by a giant impact. *Science Advances*, *5*(1), eaau3669. https://doi.org/10.1126/sciadv.aau3669

Gu, T., Fei, Y., Wu, X., & Qin, S. (2014). High-pressure behavior of Fe_3P and the role of phosphorus in planetary cores. *Earth and Planetary Science Letters*, *390*, 296–303. https://doi.org/10.1016/j.epsl.2014.01.019

Hirose, K., Wood, B., & Vočadlo, L. (2021). Light elements in the Earth's core. *Nature Reviews Earth and Environment*, *2*(9), 645–658. https://doi.org/10.1038/s43017-021-00203-6

Huang, S., Wu, X., Chariton, S., Prakapenka, V., Qin, S., & Chen, B. (2024). Thermoelastic anomaly of iron carbonitride across the spin transition and implications for planetary cores [Dataset]. *Zenodo*. https://doi.org/10.5281/zenodo.12736916

Huang, S., Wu, X., Zhu, F., Lai, X., Li, J., Neill, O. K., et al. (2021). High-pressure phase stability and thermoelastic properties of iron carbonitrides and nitrogen in the deep Earth. *Journal of Geophysical Research: Solid Earth*, *126*(6), e2021JB021934. https://doi.org/10.1029/2021JB021934

Jackson, C. R. M., Cottrell, E., Du, Z., Bennett, N. R., & Fei, Y. (2021). High pressure redistribution of nitrogen and sulfur during planetary stratification. *Geochemical Perspectives Letters*, *18*, 37–42. https://doi.org/10.7185/geochemlet.2122

Jackson, I., & Rigden, S. M. (1996). Analysis of PVT data: Constraints on the thermoelastic properties of high-pressure minerals. *Physics of the Earth and Planetary Interiors*, *96*(2–3), 85–112. https://doi.org/10.1016/0031-9201(96)03143-3

Kaminsky, F., & Wirth, R. (2017). Nitrides and carbonitrides from the lowermost mantle and their importance in the search for Earth's "lost" nitrogen. *American Mineralogist*, *102*(8), 1667–1676. https://doi.org/10.2138/am-2017-6101

Kavner, A., & Duffy, T. S. (2001). Pressure-volume-temperature paths in the laser-heated diamond anvil cell. *Journal of Applied Physics*, *89*(3), 1907–1914. https://doi.org/10.1063/1.1335827

Kresse, G., & Joubert, D. (1999). From ultrasoft pseudopotentials to the projector augmented-wave method. *Physical Review B*, *59*(3), 1758–1775. https://doi.org/10.1103/PhysRevB.59.1758

Kusakabe, M., Hirose, K., Sinmyo, R., Kuwayama, Y., Ohishi, Y., & Helffrich, G. (2019). Melting curve and equation of state of β-Fe_7N_3: Nitrogen in the core? *Journal of Geophysical Research: Solid Earth*, *124*(4), 3448–3457. https://doi.org/10.1029/2018JB015823

Lai, X., Zhu, F., Liu, J., Zhang, D., Hu, Y., Finkelstein, G. J., et al. (2018). The high-pressure anisotropic thermoelastic properties of a potential inner core carbon-bearing phase, Fe_7C_3, by single-crystal X-ray diffraction. *American Mineralogist*, *103*(10), 1568–1574. https://doi.org/10.2138/am-2018-6527

Lei, L., Zhang, L., Gao, S., Hu, Q., Fang, L., Chen, X., et al. (2018). Neutron diffraction study of the structural and magnetic properties of ε-$Fe_3N_{1.098}$ and ε-$Fe_{2.322}Co_{0.678}N_{0.888}$. *Journal of Alloys and Compounds*, *752*, 99–105. https://doi.org/10.1016/j.jallcom.2018.04.143

Lisher, E. J., Wilkinson, C., Ericsson, T., Haggstrom, L., Lundgren, L., & Wappling, R. (1974). Studies of the magnetic structure of Fe_3P. *Journal of Physics C: Solid State Physics*, *7*(7), 1344–1352. https://doi.org/10.1088/0022-3719/7/7/026

Litasov, K. D., Rashchenko, S. V., Shmakov, A. N., Palyanov, Y. N., & Sokol, A. G. (2015). Thermal expansion of iron carbides, Fe_7C_3 and Fe_3C, at 297-911 K determined by in situ X-ray diffraction. *Journal of Alloys and Compounds*, *628*, 102–106. https://doi.org/10.1016/j.jallcom.2014.12.138

Liu, J., Lin, J. F., Prakapenka, V. B., Prescher, C., & Yoshino, T. (2016). Phase relations of Fe_3C and Fe_7C_3 up to 185 GPa and 5200 K: Implication for the stability of iron carbide in the Earth's core. *Geophysical Research Letters*, *43*(24), 12–415. https://doi.org/10.1002/2016GL071353

Lv, M., Liu, J., Zhu, F., Li, J., Zhang, D., Xiao, Y., & Dorfman, S. M. (2020). Spin transitions and compressibility of ε-Fe_7N_3 and γ'-Fe_4N: Implications for iron alloys in terrestrial planet cores. *Journal of Geophysical Research: Solid Earth*, *124*(11), e2020JB020660. https://doi.org/10.1029/2020JB020660

Mashino, I., Miozzi, F., Hirose, K., Morard, G., & Sinmyo, R. (2019). Melting experiments on the Fe-C binary system up to 255 GPa: Constraints on the carbon content in the Earth's core. *Earth and Planetary Science Letters*, *515*, 135–144. https://doi.org/10.1016/j.epsl.2019.03.020

Minobe, S., Nakajima, Y., Hirose, K., & Ohishi, Y. (2015). Stability and compressibility of a new iron-nitride β-Fe_7N_3 to core pressures. *Geophysical Research Letters*, *42*(13), 5206–5211. https://doi.org/10.1002/2015GL064496

Mookherjee, M., Nakajima, Y., Steinle-Neumann, G., Glazyrin, K., Wu, X., Dubrovinsky, L., et al. (2011). High-pressure behavior of iron carbide (Fe_7C_3) at inner core conditions. *Journal of Geophysical Research: Solid Earth*, *116*(B4), B04201. https://doi.org/10.1029/2010JB007819

Nakajima, Y., Takahashi, E., Sata, N., Nishihara, Y., Hirose, K., Funakoshi, K. I., & Ohishi, Y. (2011). Thermoelastic property and high-pressure stability of Fe_7C_3: Implication for iron-carbide in the Earth's core. *American Mineralogist*, *96*(7), 1158–1165. https://doi.org/10.2138/am.2011.3703

Perdew, J. P., Burke, K., & Ernzerhof, M. (1996). Generalized gradient approximation made simple. *Physical Review Letters*, *77*(18), 3865–3868. https://doi.org/10.1103/PhysRevLett.77.3865

Prakapenka, V. B., Kubo, A., Kuznetsov, A., Laskin, A., Shkurikhin, O., Dera, P., et al. (2008). Advanced flat top laser heating system for high pressure research at GSECARS: Application to the melting behavior of germanium. *High Pressure Research*, *28*(3), 225–235. https://doi.org/10.1080/08957950802050718

Prescher, C., Dubrovinsky, L., Bykova, E., Kupenko, I., Glazyrin, K., Kantor, A., et al. (2015). High Poisson's ratio of Earth's inner core explained by carbon alloying. *Nature Geoscience*, *8*(3), 220–223. https://doi.org/10.1038/ngeo2370

Prescher, C., & Prakapenka, V. B. (2015). Dioptas: A program for reduction of two-dimensional X-ray diffraction data and data exploration. *High Pressure Research*, *35*(3), 223–230. https://doi.org/10.1080/08957959.2015.1059835

Tagawa, S., Gomi, H., Hirose, K., & Ohishi, Y. (2022). High-temperature equation of state of FeH: Implications for hydrogen in Earth's inner core. *Geophysical Research Letters*, *49*(5), e2021GL096260. https://doi.org/10.1029/2021GL096260

Thompson, S., Komabayashi, T., Breton, H., Suehiro, S., Glazyrin, K., Pakhomova, A., & Ohishi, Y. (2020). Compression experiments to 126 GPa and 2500 K and thermal equation of state of Fe_3S: Implications for Sulphur in the Earth's core. *Earth and Planetary Science Letters*, *534*, 116080. https://doi.org/10.1016/j.epsl.2020.116080

Toby, B. H. (2001). EXPGUI, a graphical user interface for GSAS. *Journal of Applied Crystallography*, *34*(2), 210–213. https://doi.org/10.1107/S0021889801002242

Tsuzuki, A., Sago, S., Hirano, S. I., & Naka, S. (1984). High temperature and pressure preparation and properties of iron carbides Fe_7C_3 and Fe_3C. *Journal of Materials Science*, *19*(8), 2513–2518. https://doi.org/10.1007/BF00550805

Wood, B. J. (1993). Carbon in the core. *Earth and Planetary Science Letters*, *117*(3–4), 593–607. https://doi.org/10.1016/0012-821X(93)90105-I

Zhou, Y., Dong, Z. Y., Hsieh, W. P., Goncharov, A. F., & Chen, X. J. (2022). Thermal conductivity of materials under pressure. *Nature Reviews Physics*, *4*(5), 319–335. https://doi.org/10.1038/s42254-022-00423-9

References From the Supporting Information

Liu, J., Li, J., & Ikuta, D. (2016). Elastic softening in Fe_7C_3 with implications for Earth's deep carbon reservoirs. *Journal of Geophysical Research: Solid Earth*, *121*(3), 1514–1524. https://doi.org/10.1002/2015JB012701

Zhu, F., Li, J., Walker, D., Liu, J., Lai, X., & Zhang, D. (2019). Origin and consequences of non-stoichiometry in iron carbide Fe_7C_3. *American Mineralogist*, *104*(3), 325–332. https://doi.org/10.2138/am-2019-6672